Polymer 49 (2008) 2492–2506

Contents lists available at ScienceDirect

Polymer

journal homepage: www.elsevier.com/locate/polymer

Effect of the ratio of maleated polypropylene to organoclay on the structure and properties of TPO-based nanocomposites. Part II: Thermal expansion behavior

Do Hoon Kim [a], Paula D. Fasulo [b], William R. Rodgers [b], D.R. Paul [a,*]

[a] Department of Chemical Engineering, Texas Materials Institute, The University of Texas at Austin, Austin, TX 78712-1062, United States
[b] General Motors Research and Development Center, 30500 Mound Road, Warren, MI 48090, United States

ARTICLE INFO

Article history:
Received 25 January 2008
Received in revised form 2 April 2008
Accepted 3 April 2008
Available online 8 April 2008

Keywords:
Polymer nanocomposites
Thermal expansion
TPO

ABSTRACT

Significant reductions in linear thermal expansion coefficients in the flow and transverse directions of injection-molded specimens of thermoplastic polyolefin, or TPO, nanocomposites were achieved by controlling the maleated polypropylene (PP-*g*-MA)/organoclay ratio. Linear thermal expansion behavior was examined using a thermomechanical analyzer (TMA). The trends in thermal expansion for the nanocomposites are discussed in terms of the morphology of both dispersed clay and elastomer phases by means of transmission electron microscopic (TEM) and atomic force microscopic (AFM) observations and subsequent particle analyses. A higher PP-*g*-MA/organoclay ratio causes an increase in the aspect ratio of clay particles along the flow direction (FD) and transverse direction (TD) for the injection-molded specimens; however, the aspect ratio along the FD was higher than that along the TD. On the other hand, the aspect ratio of elastomer particles along the FD was much higher than that along the TD. Furthermore, highly elongated elastomer particles along the FD were observed. The combined effect of the mechanical constraint by organoclay and the highly elongated elastomer particles caused at high PP-*g*-MA contents was responsible for the significant reduction of thermal expansion for these materials.

1. Introduction

The interest in polymer/layered silicate nanocomposites stems from the possibility that only a few percent of clay can lead to significant improvements in stiffness and strength, gas barrier properties, and other physical properties [1–7].

A particularly promising benefit of incorporating layered silicates into polymers is the reduction of the thermal expansion coefficient (CTE) and improved dimensional stability. The large discrepancy in the CTE between most polymers, e.g., $\sim 10^{-4}$ mm/mm °C for polypropylene (PP) [8], and metals ($\sim 10^{-5}$ mm/mm °C) is a significant impediment in replacing metal parts with light weight plastic parts in various automotive applications. Because of the high modulus and low thermal expansion coefficient of the layered silicate filler, the linear thermal expansion of nanocomposites can be significantly decreased by simple mechanical restraints considerations provided the clay platelets are well-dispersed in the polymer matrix (high aspect ratio) and appropriately oriented [2,9–14]. The same factors lead to effective reinforcement at low loading for nanocomposites based on the clay-mineral montmorillonite (MMT). The small absolute size of filler particles leads to a better surface finish than that expected for conventional composites [15]. Numerous studies have examined how filler shape, size, concentration, and dispersion influence the thermal expansion of polymer composites [9–14,16–19]. Despite the practical importance of thermal expansion characteristics, relatively few studies have systematically investigated the relationship between morphology and dimensional stability, e.g., CTE, of polymer/clay nanocomposites [13,14,20]. Recently, our laboratory reported on the anisotropic thermal expansion behavior and the morphology for the nanocomposites based on nylon 6 and those formed by blending polypropylene with an ethylene–octene elastomer for toughening and a masterbatch mixture containing equal parts of maleated polypropylene (PP-*g*-MA) and an organoclay for reinforcement and dispersion [13,14].

Polyolefin/layered silicate nanocomposites, especially PP, have been widely investigated for replacement of metals and high performance engineering thermoplastics [21–33]. However, nonpolar PP does not inherently lead to a high level of dispersion of organoclays. Therefore, it has been found useful to add small amounts of maleated PP or PP-*g*-MA, to serve as a "compatibilizer" to achieve better dispersion of the silicate platelets in the PP or

* Corresponding author. Tel.: +1 512 471 5392; fax: +1 512 471 0542.
E-mail address: drp@che.utexas.edu (D.R. Paul).

0032-3861/$ – see front matter © 2008 Elsevier Ltd. All rights reserved.
doi:10.1016/j.polymer.2008.04.005

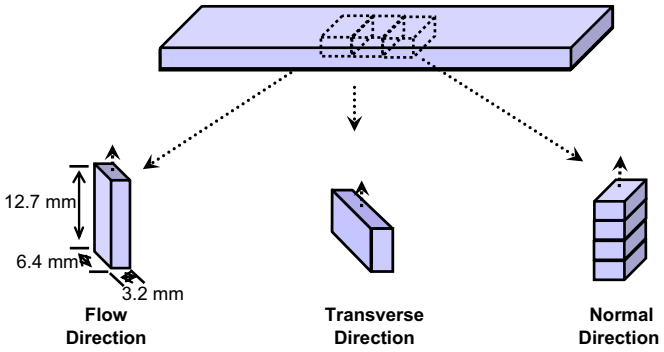

Fig. 1. Schematic diagram of the sampling for thermal expansion measurement.

thermoplastic olefin (TPO) matrix and, as a consequence, improve reinforcement. Interestingly, very few studies have reported on how the ratio of PP-*g*-MA to organoclay affects morphology and the performance of PP-based nanocomposites [28,32,33] or TPO-based nanocomposites [34,35]. Recently, we reported the effect of the PP-*g*-MA/organoclay ratio on the morphology and performance, e.g., mechanical, rheological and thermal expansion behavior, for PP-based nanocomposites that contained no elastomer phase [20].

The purpose of this paper is to examine the effect of PP-*g*-MA/organoclay ratio on morphology and thermal expansion behavior of TPO nanocomposites. The first paper in this series described the effect of PP-*g*-MA/organoclay ratio on mechanical, rheological properties, and morphology of the same TPO-based nanocomposites [36]. An in-depth particle analysis of both filler (from TEM images) and elastomer (from AFM images) morphology along the flow and transverse directions of injection-molded specimens is used to evaluate how these phases influence thermal expansion behavior. As expected, the ratio of PP-*g*-MA to organoclay strongly affects the morphology of clay platelets and elastomer particles resulting in changes in the thermal expansion characteristics. A better understanding of the influence of PP-*g*-MA/organoclay ratio on the relationship between composite morphology and CTE behavior is needed to achieve improved dimensional stability of injection-molded parts for TPO-based nanocomposites. A subsequent paper will attempt to model the stiffness and thermal expansion of these nanocomposites as a function of MMT content and PP-*g*-MA/organoclay ratio.

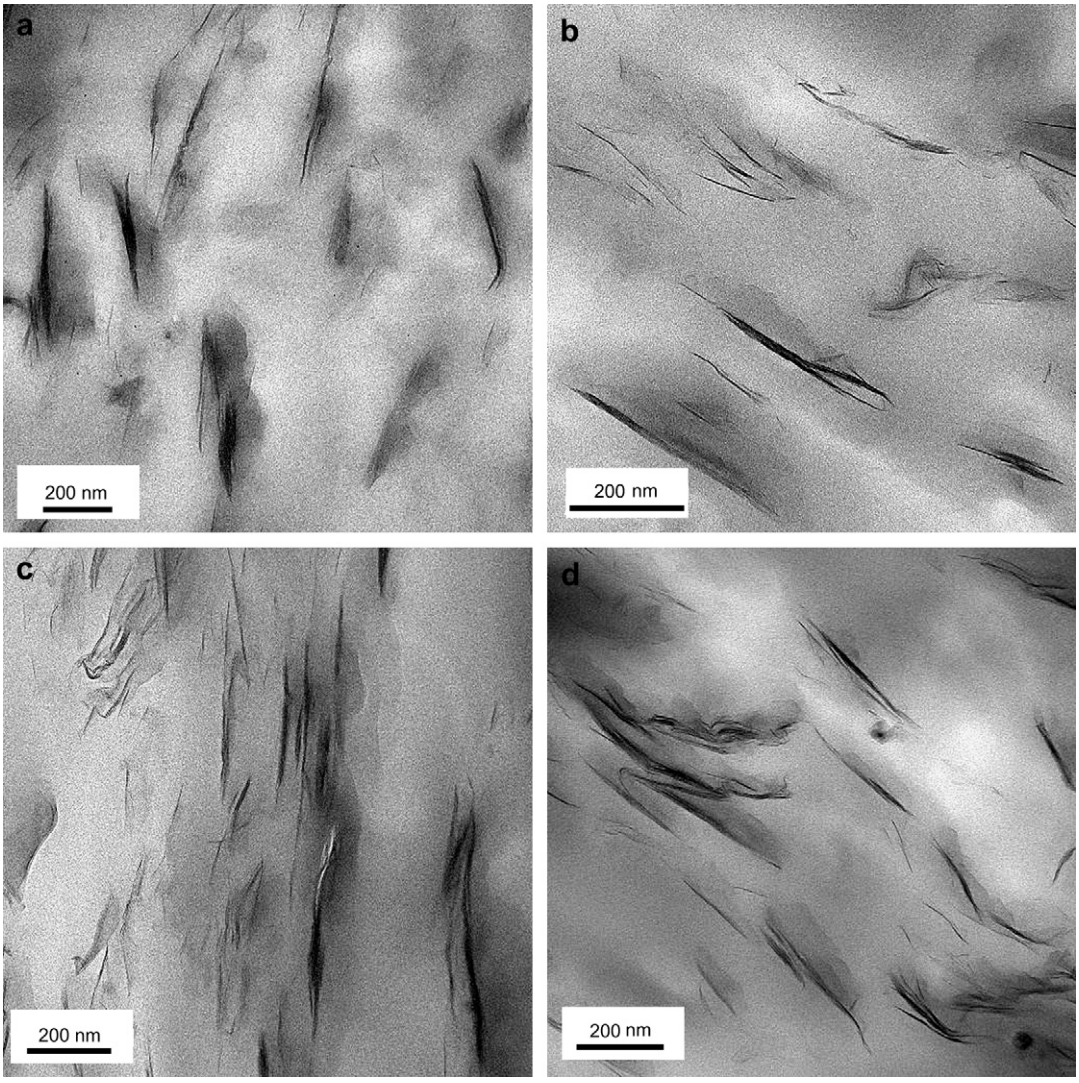

Fig. 2. TEM images of TPO-based nanocomposites showing clay particle morphology as a function of MMT content of 3 (a and b), and 5 wt% (c and d) at a fixed PP-*g*-MA/organoclay ratio of 1.0. Images were taken from the core and viewed parallel to the TD (a and c) and FD (b and d).

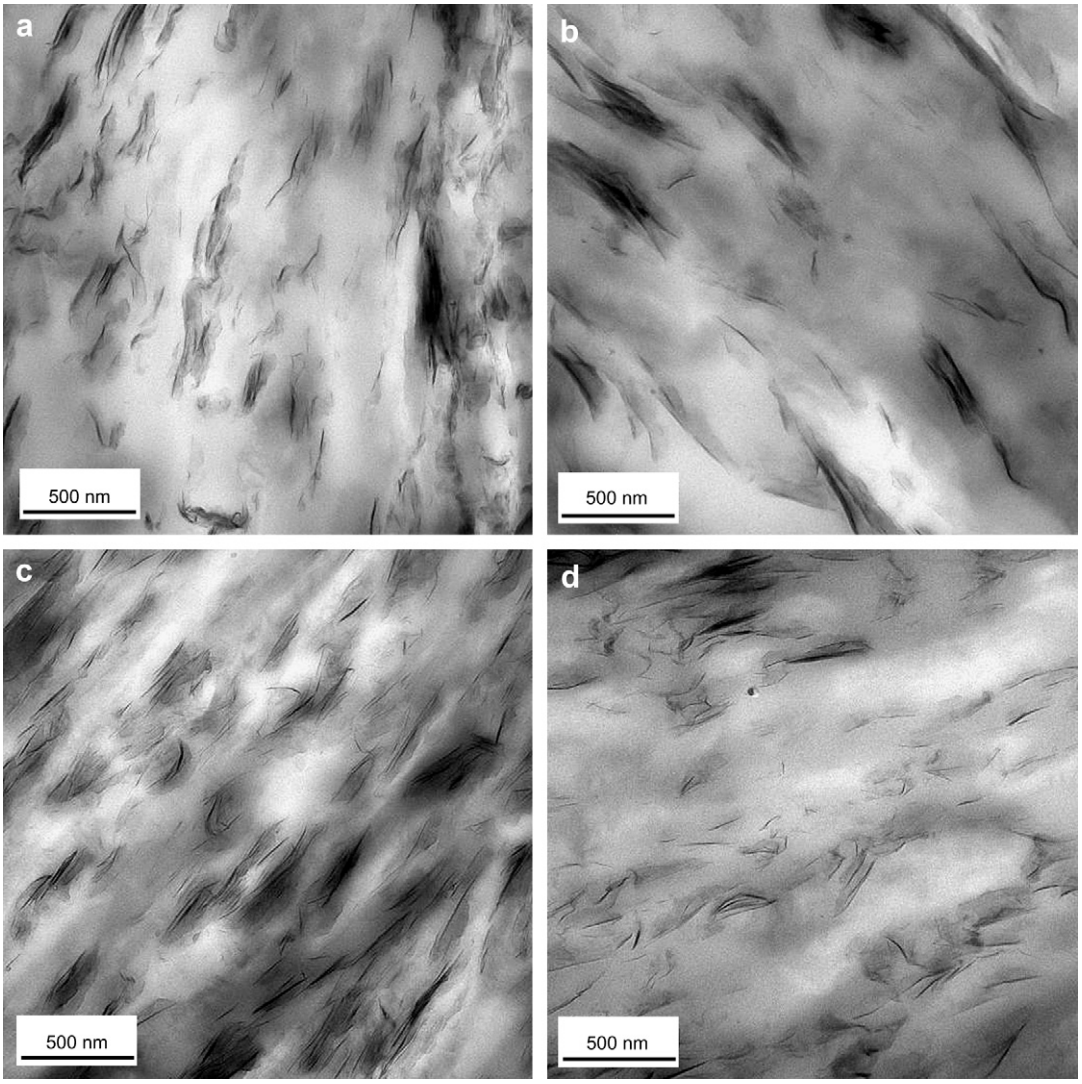

Fig. 3. TEM images of TPO-based nanocomposites showing clay particle morphology as a function of a ratio of PP-*g*-MA to organoclay of 0.5 (a and b), and 2.0 (c and d) at a fixed MMT content of 5 wt%. Images were taken from the core and viewed parallel to the TD (a and c) and FD (b and d).

2. Experimental

2.1. Materials and composite preparation

Nanocomposites were formed by melt compounding mixtures of a commercial TPO (CA 387 from Basell Polyolefins, melt index = 17 g/10 min), polypropylene-grafted maleic anhydride (PP-*g*-MA, MA content = 1.0 wt%) and an organoclay (di-methyl, dihydrogenated tallow-montmorillonite). The nanocomposite pellets were dried and then injection molded into standard tensile (ASTM D638, Type I) and Izod (ASTM D256) specimens. Further details of the melt processing steps used to form and shape these materials are given in the first paper in this series [36].

2.2. Morphological characterization

Samples for transmission electron microscopic (TEM) analysis were taken from the central region of a 13 cm Izod bar, located parallel and perpendicular to the flow direction, about 3–4 cm away from the far end halfway between the top and the bottom surfaces of the bar. Sections taken from molded bars were viewed in the three orthogonal directions, flow direction (FD), transverse direction (TD), and normal direction (ND). The detailed geometry of the specimen and the viewing directions for TEM are described elsewhere [13,37–39]. The ultra-thin sections, ranging from 50 to 70 nm in thickness, were cryogenically cut with a diamond knife at temperatures of −65 °C for the specimen and −58 °C for the knife using an RMC PowerTome XL ultramicrotome with a CR-X universal cryosectioning system. Sections were collected on 300 mesh copper TEM grids and subsequently dried with filter paper. The sections were examined using a JEOL 2010F TEM with a LaB_6 filament operating at an accelerating voltage of 120 kV.

Atomic force microscopic (AFM) experiments were performed on cryogenically microtomed surfaces of nanocomposites containing elastomer using a Digital Instruments Dimension 3100 with Nanoscope IV controller at room temperature. Images were recorded in the tapping mode using etched silicon probes. The instrumental parameters such as the set point and the gain were adjusted to improve the image resolution. The particle analysis of the elastomer phase obtained by AFM images used a similar procedure as given in the first paper in this series [36].

2.3. Thermal expansion measurement

Thermal expansion tests were conducted according to ASTM D696 using a Perkin–Elmer thermomechanical analyzer (TMA 7).

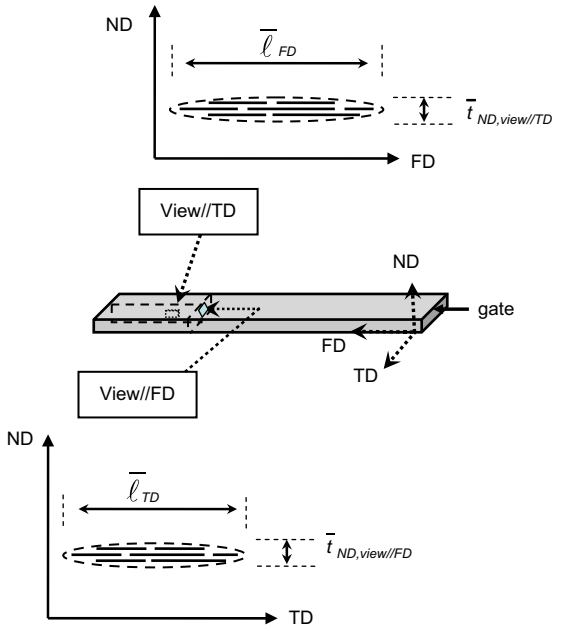

Fig. 4. Schematic illustration of clay particle length and thickness obtained from TEM images in the different flow directions.

Rectangular specimens were prepared from the central region of Izod bars. The dimensions of the specimens were as follows: thickness = 3.2 mm, width = 6.4 mm, and height = 12.7 mm. Thermal expansion measurements were made in all three orthogonal directions, i.e., flow direction (FD), transverse direction (TD), and normal direction (ND) (see Fig. 1). Due to the thickness of the injection-molded specimens, measurements made in the ND were performed on a stack of four specimens that were glued together using an instant adhesive. Each specimen was held at −40 °C for 5 min, followed by heating at a rate of 5 °C/min to 125 °C and subsequently held for 30 min, and then quenched to room temperature. In order to assess both reversible and non-reversible effects, each specimen was stored at room temperature for at least 24 h after the first heating and, then re-heated at a rate of 5 °C/min to 125 °C. All measurements were made in a nitrogen atmosphere.

3. Results and discussion

3.1. Morphological characterization and particle analysis using TEM and AFM

3.1.1. Clay particle analysis

As shown in previous papers [20,36], a high aspect ratio of clay particles contributes to greater increase in modulus and greater reduction in thermal expansion and is related to the degree of clay dispersion. A few studies have indicated that the shape of the MMT particles may be anisotropic, i.e., different lengths along the FD and TD, based on the morphology and/or thermal expansion behavior of the nanocomposites [13,14,39–42].

Figs. 2 and 3 show TEM micrographs for TPO-based nanocomposites with various MMT contents and PP-*g*-MA/organoclay ratios as viewed parallel to the FD and to the TD. The length of clay

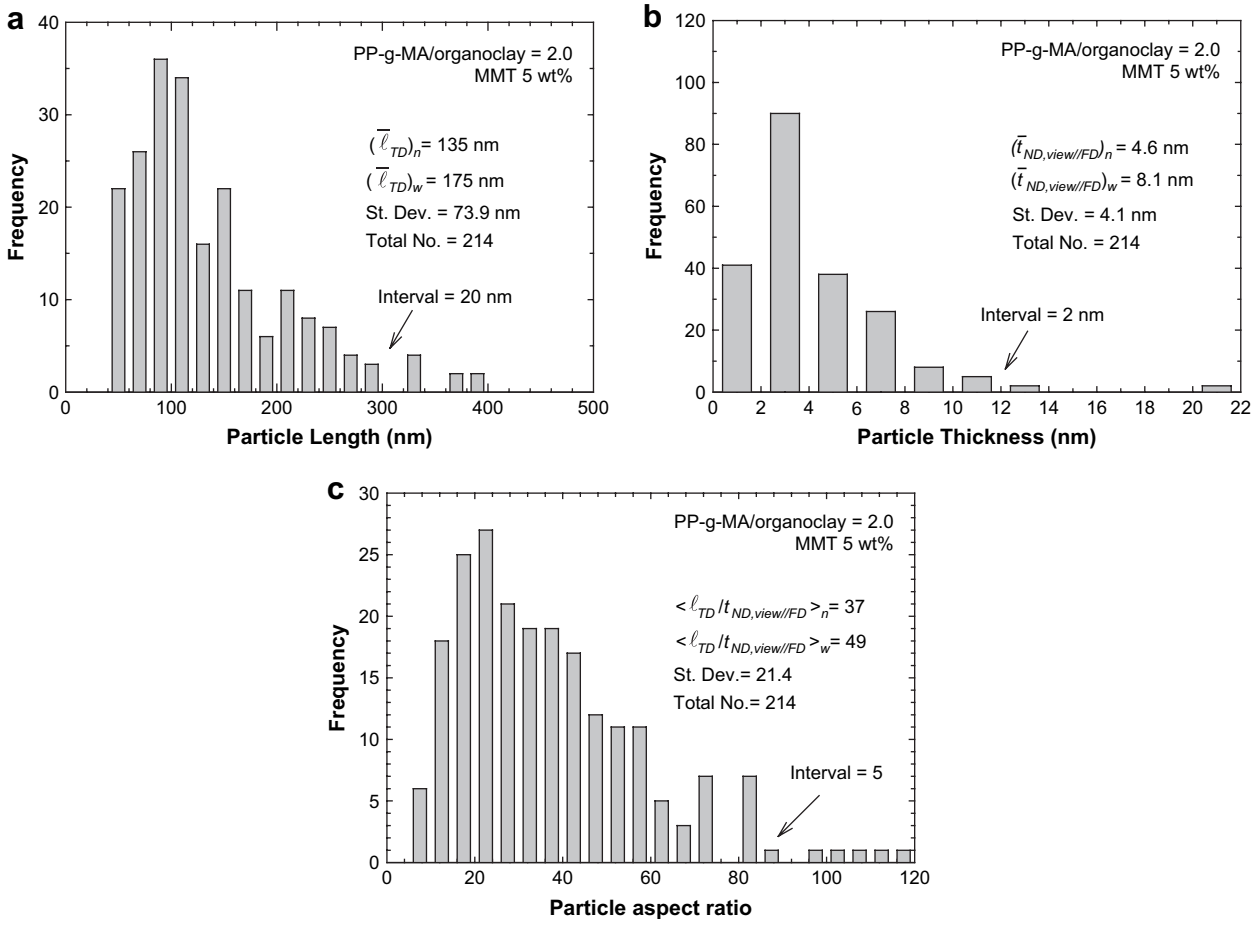

Fig. 5. Histogram of MMT particle dimensions for TPO/PP-*g*-MA/MMT nanocomposites containing 5 wt% of MMT at a PP-*g*-MA/organoclay ratio of 2.0, viewed parallel to FD: particle length (a), particle thickness (b) and particle aspect ratio (c).

Table 1
Image analysis results of clay particles obtained from TEM images of TPO/PP-*g*-MA/MMT nanocomposites for different MMT contents at a fixed ratio of PP-*g*-MA/organoclay of 1.0

MMT (wt%)	Plane of viewing	Number average particle length (nm), $\bar{\ell}_n$	Weight average particle length (nm), $\bar{\ell}_w$	Number average particle thickness (nm), $\bar{t}_n$	Weight average particle thickness (nm), $\bar{t}_w$	Number average aspect ratio, $\langle \ell/t \rangle_n$	Weight average aspect ratio, $\langle \ell/t \rangle_w$	Aspect ratio	
								$\bar{\ell}_n/\bar{t}_n$ [a]	$\bar{\ell}_w/\bar{t}_w$ [b]
0.84	FD–ND	178	222	5.1	8.2	46	63	35	27
	TD–ND	147	181	4.4	7.6	44	57	33	24
2.6	FD–ND	165	225	5.6	10.4	40	59	29	22
	TD–ND	141	174	4.4	8.7	43	53	32	29
4.7	FD–ND	152	185	5.8	10.9	38	51	26	17
	TD–ND	141	167	5.1	8.0	35	44	27	21
6.8	FD–ND	134	178	5.7	10.8	32	43	24	17
	TD–ND	133	171	5.1	8.6	34	44	26	20

[a] The values of the aspect ratio were computed from the number average particle length and thickness.
[b] The values of the aspect ratio were computed from the weight average particle length and thickness.

Table 2
Image analysis results of clay particles obtained from TEM images of TPO/PP-*g*-MA/MMT nanocomposites for different PP-*g*-MA/organoclay ratios at a fixed MMT content of 5 wt%

PP-*g*-MA/ organoclay	Plane of viewing	Number average particle length (nm), $\bar{\ell}_n$	Weight average particle length (nm), $\bar{\ell}_w$	Number average particle thickness (nm), $\bar{t}_n$	Weight average particle thickness (nm), $\bar{t}_w$	Number average aspect ratio, $\langle \ell/t \rangle_n$	Weight average aspect ratio, $\langle \ell/t \rangle_w$	Aspect ratio	
								$\bar{\ell}_n/\bar{t}_n$ [a]	$\bar{\ell}_w/\bar{t}_w$ [b]
0	FD–ND	623	1553	84.1	134.6	9	10	12	7
	TD–ND	447	762	90.2	196.5	7	10	5	4
0.5	FD–ND	161	214	13.9	21.3	16	34	12	10
	TD–ND	181	227	12.8	22.3	17	22	14	10
1.0	FD–ND	152	185	5.8	10.9	38	51	26	17
	TD–ND	141	167	5.1	8.0	35	44	27	21
2.0	FD–ND	143	187	4.1	7.5	42	52	34	25
	TD–ND	135	175	4.6	8.2	37	49	29	21

[a] The values of the aspect ratio were computed from the number average particle length and thickness.
[b] The values of the aspect ratio were computed from the weight average particle length and thickness.

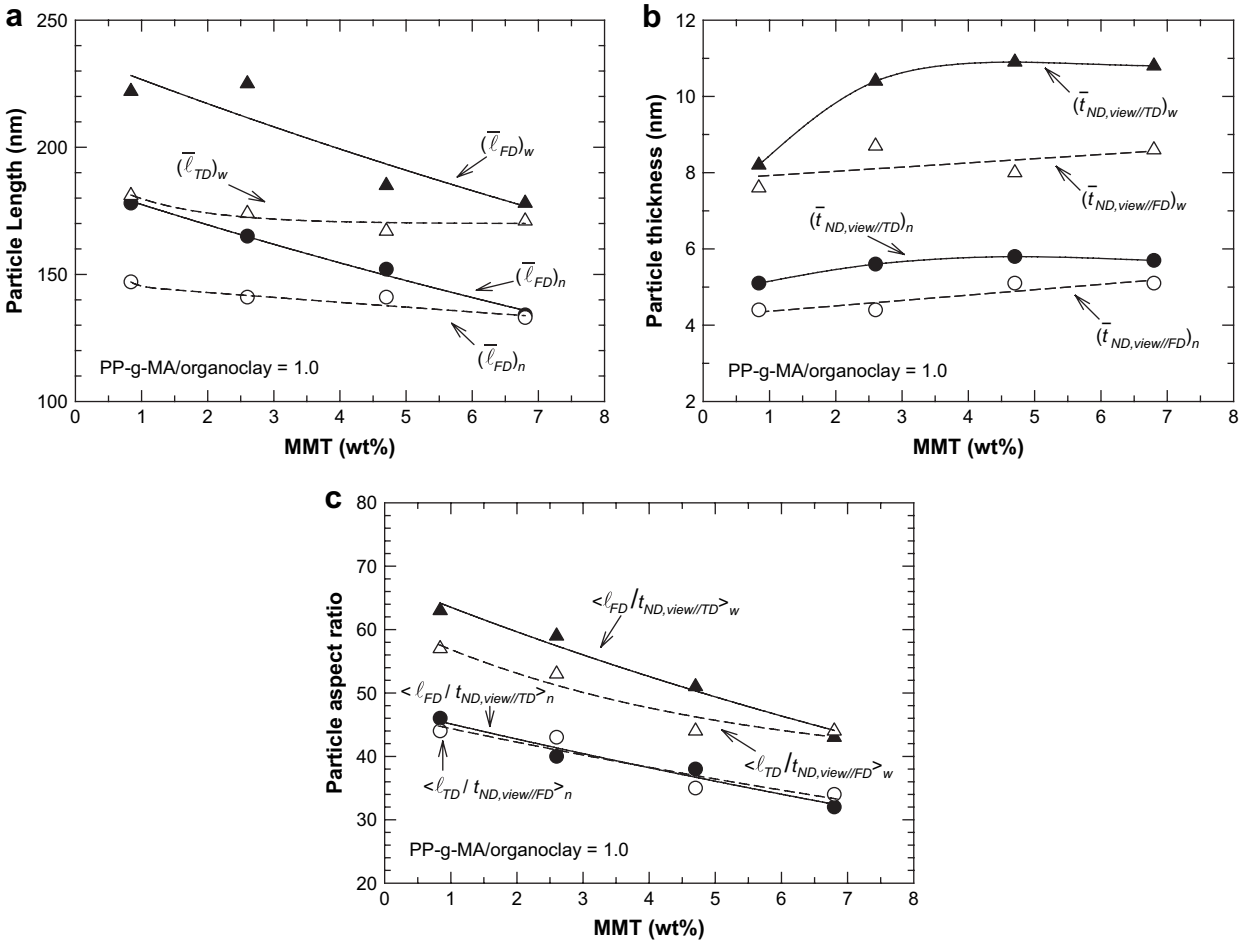

Fig. 6. The effect of MMT content on particle length (a), thickness (b) and aspect ratio (c) of TPO/PP-*g*-MA/MMT nanocomposites at a fixed PP-*g*-MA/organoclay ratio of 1.0.

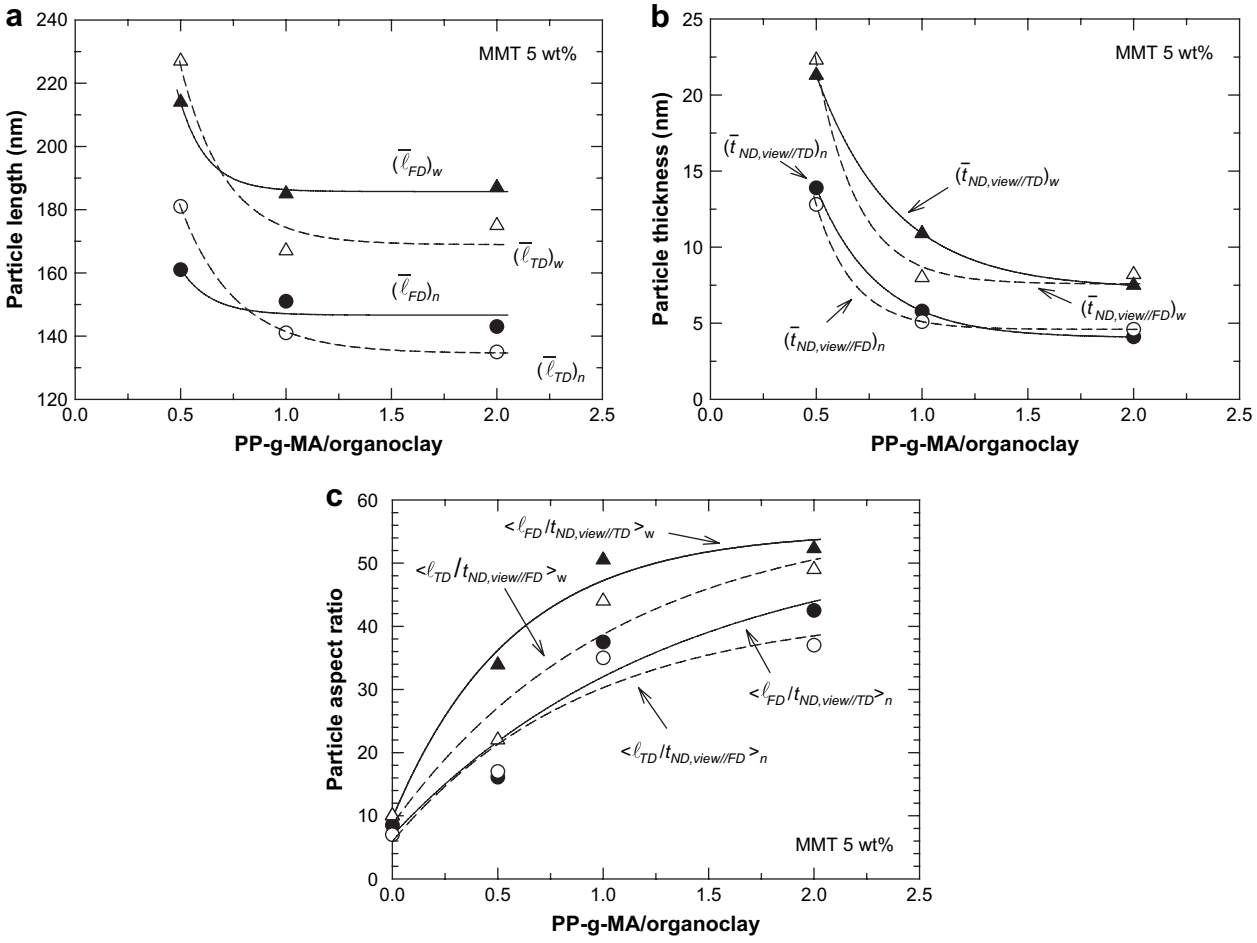

Fig. 7. Comparison of clay particle length (a), thickness (b) and aspect ratio (c) with TPO/PP-*g*-MA/MMT nanocomposites in the different flow directions.

particles seems to be shorter in views parallel to FD than those parallel to TD irrespective of MMT content and PP-*g*-MA/organoclay ratio; the thickness of the particles shows somewhat different tendencies. In views parallel to the FD the particles seem to be thinner than those parallel to the TD at a fixed PP-*g*-MA ratio of 1.0 (see Fig. 2); whereas, at a fixed MMT content (see Fig. 3) the particles seem to be thicker in views parallel to the FD than those parallel to the TD. Furthermore, the alignment of the clay particles shows different trends. At low MMT contents, e.g., 3 wt%, the alignment and dispersion of the clay particles as seen along the TD seem to be better than those along the FD. At higher MMT content like 5 wt%, the alignment and dispersion of clay particles in the two directions appear similar. On the other hand, at the low PP-*g*-MA/organoclay ratio of 0.5, the particles seem to be similar or a little thicker in views parallel to FD than those parallel to TD; whereas, the trend seems opposite at the higher ratio of 2.0. These trends may reflect differences in the flow field during the injection-molding process.

Clay particle analyses were performed to quantify the trends described above. Fig. 4 illustrates the nomenclature used to describe the length and thickness of clay particles in the two different viewing directions. In our laboratory, a sizeable effort has been devoted to perform in-depth particle analysis using TEM photomicrographs to provide quantitative information regarding the relationship between clay structure and nanocomposite properties [14,37–39,43,44]. As seen in the histograms in Fig. 5, there is a sizeable distribution in particle length and thickness as well as in aspect ratio. As reported in previous papers [20,36], the distribution in particle aspect ratio can be obtained by calculating the aspect ratio of individual clay particles. From such histograms, number and weight average values of particle length, thickness and aspect ratio with varying MMT contents and/or PP-*g*-MA/organoclay ratios were determined and are summarized in Tables 1 and 2 and in Figs. 6 and 7. In some cases, the averages of the particle dimensions obtained from views parallel to the FD and TD are essentially the same but meaningful differences between the two views exist in some cases. The data obtained from the view in the FD–ND plane are taken from the previous paper [36], while those from the view in the TD–ND plane are reported here.

Fig. 6(a) and (b) shows the length and thickness of clay particles versus MMT content at a fixed ratio of PP-*g*-MA/organoclay = 1.0. While the particle length along the FD, $\bar{\ell}_{FD}$ (obtained in a view parallel to the TD), decreases sharply as MMT content increases, along the TD the observed length, $\bar{\ell}_{TD}$, decreases less. The thickness of the clay particles increases with increasing MMT content in nanocomposites regardless of viewing direction or method of averaging; however, the thickness measured in views parallel to the TD, $\bar{t}_{ND,view||TD}$, is consistently greater than that in views parallel to the FD, $\bar{t}_{ND,view||FD}$. Consequently, the average aspect ratio of the clay particles, Fig. 6(c), decreases on addition of MMT. The weight average aspect ratios along the FD, $\langle \ell_{FD}/t_{ND,view||TD} \rangle_w$, appear somewhat larger than those along the TD, $\langle \ell_{TD}/t_{ND,view||FD} \rangle_w$; the differences in the number average aspect ratios between the two viewing directions are not as great. This is one of the main reasons for the greater reduction of thermal expansion coefficient along the FD than the TD since a higher aspect ratio of the filler should lead to

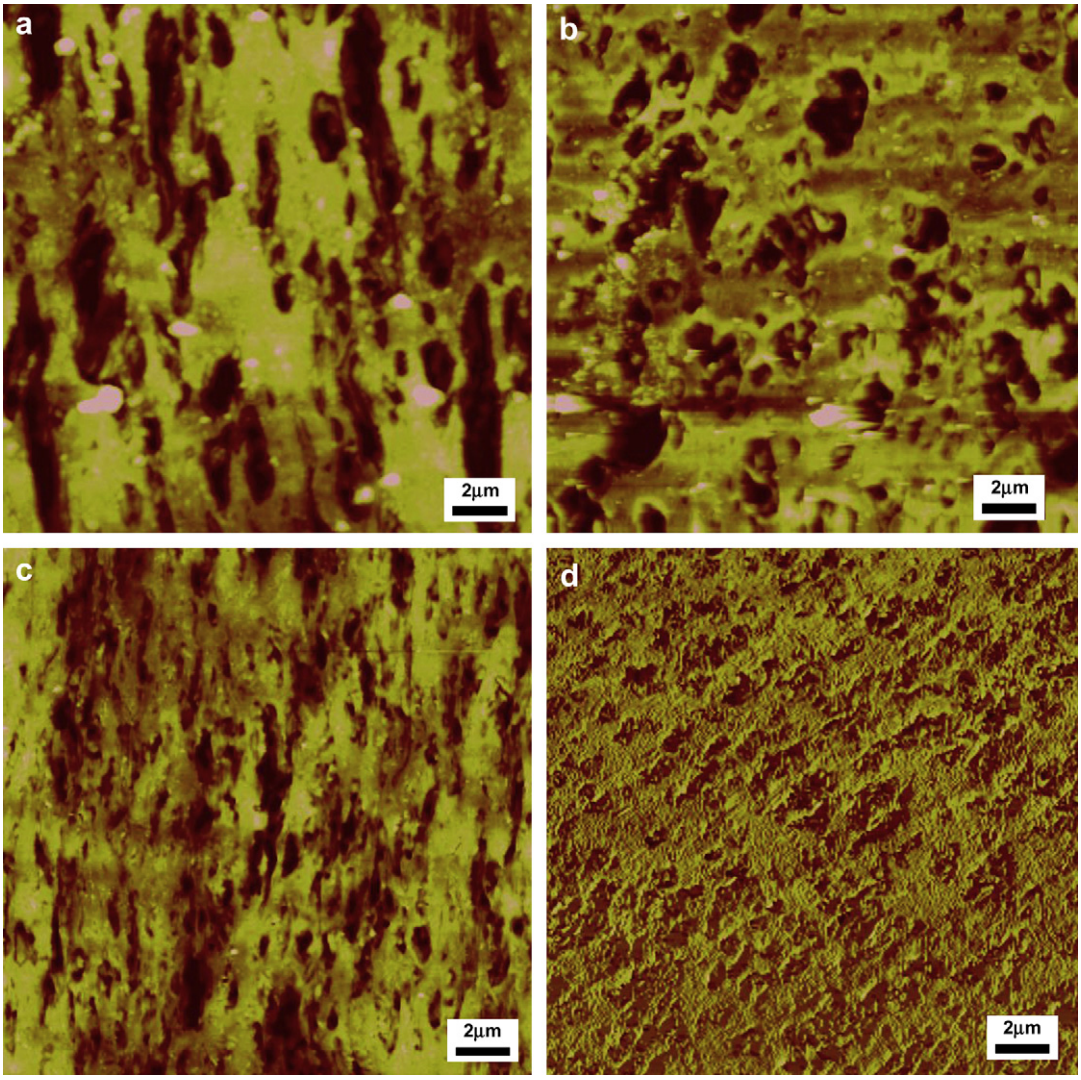

Fig. 8. AFM images of TPO-based nanocomposites showing elastomer particle morphology as a function of MMT content of 1 (a and b), and 5 wt% (c and d) at a fixed PP-*g*-MA/organoclay ratio of 1.0. Images were taken from the core and viewed parallel to the TD (a and c) and FD (b and d).

a lower thermal expansion coefficient (CTE) as reported for nylon-based nanocomposite [13]. The other possibility is the degree of orientation of clay platelets to the flow direction. When we compared the orientation of clay particles along the FD (see Fig. 2(a) and (c)) and TD (Fig. 2(b) and (d)), the degree of orientation along the FD is somewhat higher than that along the TD. The higher aspect ratio coupled with orientation of clay platelets should lead to a lower thermal expansion coefficient. We will deal with this issue in detail in a subsequent paper.

From Fig. 7 it was found that the number and weight averages of the length and thickness of clay particles at a fixed MMT content of 5 wt% decrease as the PP-*g*-MA/organoclay ratio increases irrespective of the direction of viewing. Since the change of particle thickness is much greater than that of the particle length, the particle aspect ratio increases as the PP-*g*-MA/organoclay ratio increases as shown in Fig. 7(c). The particles are somewhat longer when viewed along the FD, $\bar{\ell}_{FD}$, than when viewed along the TD, $\bar{\ell}_{TD}$; whereas, the particle thicknesses in the two views are rather similar as the PP-*g*-MA/organoclay ratio increases. This suggests that the particle aspect ratio, $\langle \ell/t \rangle_w$, along the FD is higher than that along the TD.

Lee et al. [14] reported that the aspect ratio along the TD is larger than that along the FD for PP/elastomer nanocomposites containing equal parts of PP-*g*-MA and organoclay. This discrepancy with the current observations may stem from several sources including the difference in mixing methods. Lee et al. mixed the PP, elastomer and a masterbatch containing equal parts of PP-*g*-MA and an organoclay; whereas, we mixed TPO, PP-*g*-MA and organoclay at the same time. When we mixed TPO with same masterbatch, we could observe similar behaviors as Lee et al., e.g., the aspect ratio along the TD is somewhat higher than that along the FD. Moreover, the clay particles along the FD seem to be more skewed than those along the TD. The difference in morphology caused by the mixing protocol for TPO-based nanocomposites will be discussed in more detail in a subsequent paper. On the other hand, the aspect ratio used in their study was calculated by ratio of the average particle length and the average particle thickness, i.e., $\bar{\ell}/\bar{t}$; whereas, the aspect ratio here is the average of individual particle aspect ratios, $\langle \ell/t \rangle$, as mentioned above. However, some measures of aspect ratio, e.g., $\bar{\ell}_n/\bar{t}_n$ and $\bar{\ell}_w/\bar{t}_w$, show a marginal difference; the aspect ratio along the TD shows higher values than that along the FD. We believe this is related to the way the aspect ratio is calculated and should be treated carefully in order to analyze the mechanical and thermal properties of these nanocomposites. This issue will be discussed in more detail in the subsequent paper dealing with modeling of the properties of these nanocomposites.

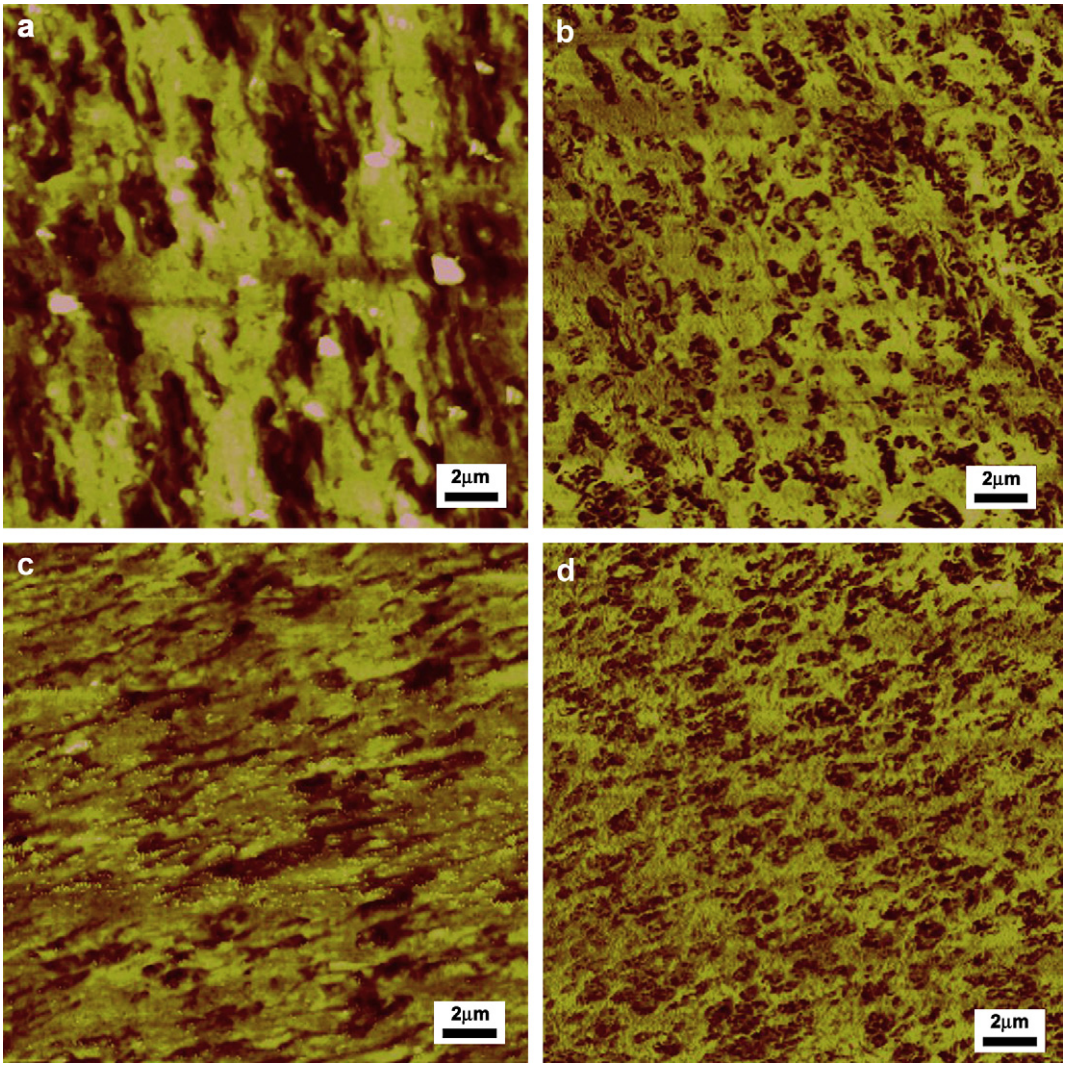

Fig. 9. AFM images of TPO-based nanocomposites showing elastomer particle morphology as a function of a ratio of PP-*g*-MA to organoclay of 0.5 (a and b) and 2.0 (c and d) at a fixed MMT content of 5 wt%. Images were taken from the core and viewed parallel to the TD (a and c) and FD (b and d).

3.1.2. *Elastomer particle analysis*

Figs. 8 and 9 show AFM images that reveal the elastomer morphology of TPO nanocomposites as a function of MMT content, the ratio of PP-*g*-MA/organoclay, and viewing plane. As MMT content increases, the elastomer particles become slightly smaller irrespective of viewing plane. However, the elastomer particles seem more oriented in views in the FD–ND plane than those in the TD–ND plane. Furthermore, the elongation of elastomer particles is much greater in views in the FD–ND plane than those in the TD–ND plane as shown in Fig. 8. Similar trends are seen as the PP-*g*-MA/organoclay ratio increases. As shown in Fig. 9, the elastomer particles seem to become somewhat smaller and more elongated when viewed in the FD–ND plane than when viewed in the TD–ND plane as the PP-*g*-MA/organoclay ratio increases. Interestingly, the size of the elastomer particles, when viewed in the FD, decreases as the PP-*g*-MA/organoclay ratio increases; whereas, the size observed in the TD does not change much. Furthermore, the elastomer particles are more aligned along the FD than along the TD as might be expected.

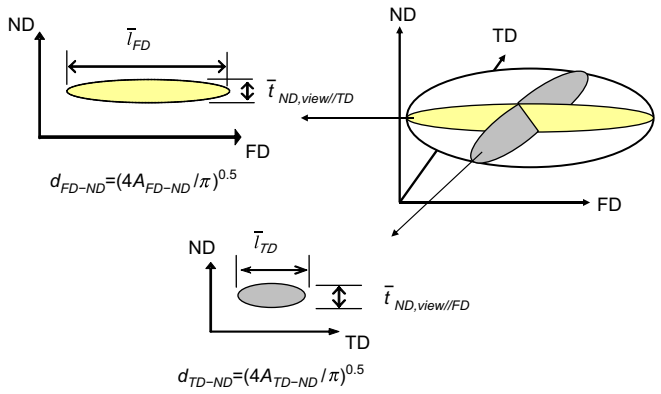

Fig. 10. Schematic illustration of elastomer particle length and thickness obtained from AFM images plus definition of average particle diameter calculated from observed particle area.

Particle analyses were performed to quantify these observations. Fig. 10 shows a schematic illustration of elongated elastomer particles and the nomenclature used to quantify their length and thickness obtained from AFM images [14]. Fig. 11 shows histograms of apparent particle diameter, length, thickness and aspect ratio from views in the TD–ND plane at fixed PP-*g*-MA/organoclay ratio of 2.0 and MMT content of 5.0 wt%. A summary of the elastomer particle size analyses, expressed as number and

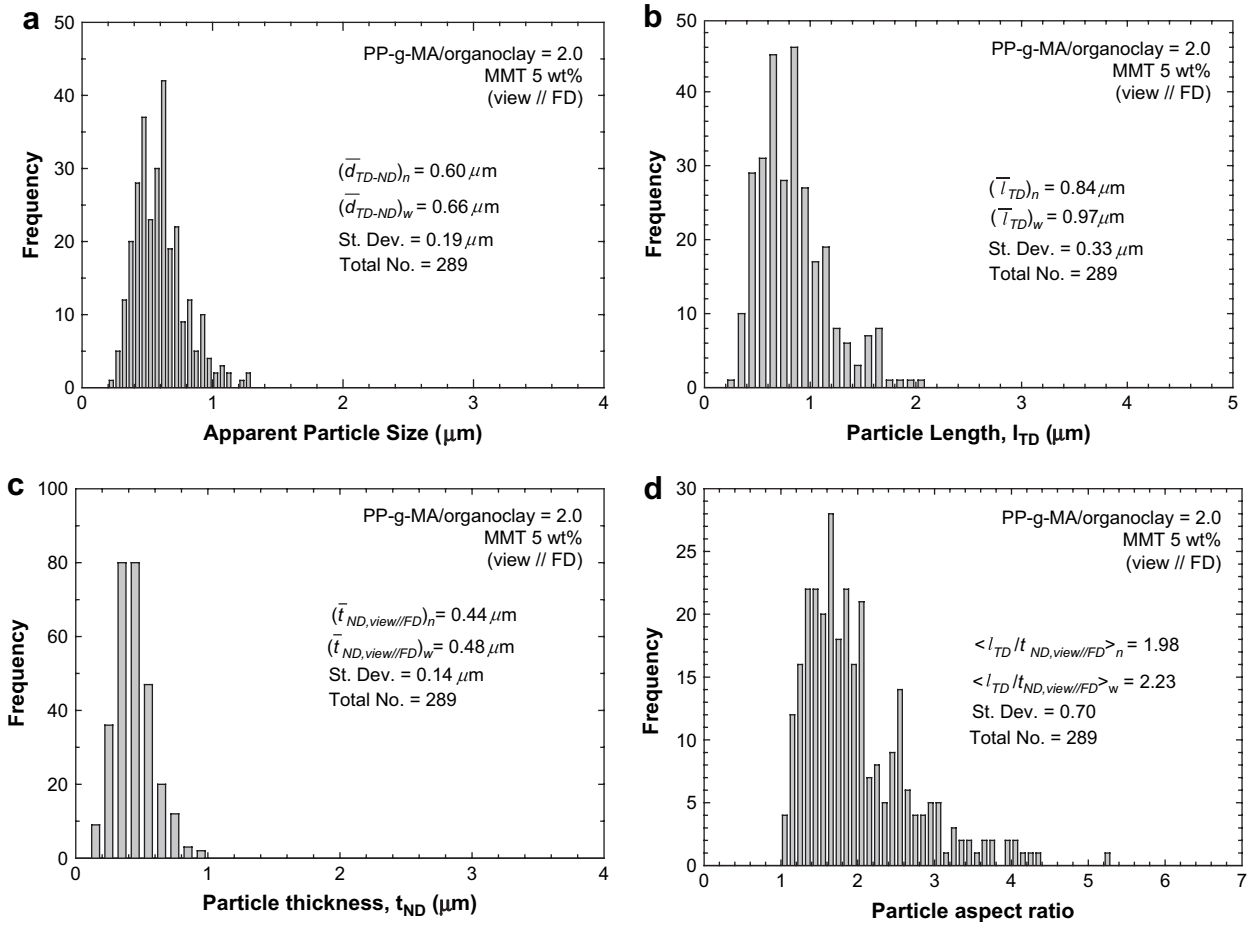

Fig. 11. Histograms of apparent elastomer particle size (a), length (b), thickness (c) and aspect ratio (d) data obtained by analyzing AFM images of TPO/PP-*g*-MA/MMT nanocomposites with the ratio of PP-*g*-MA to organoclay of 2.0 at a fixed MMT contents of 5 wt% (viewed parallel to FD).

Table 3
Elastomer particle size comparison of TPO/PP-*g*-MA/MMT nanocomposites for different MMT contents at a fixed ratio of PP-*g*-MA/organoclay of 1.0

MMT (wt%)	Plane of viewing	Particle size (μm)		Major length (μm)		Minor length (μm)		Elastomer aspect ratio			
		$\bar{d}_n$	$\bar{d}_w$	$\bar{\ell}_n$	$\bar{\ell}_w$	$\bar{t}_n$	$\bar{t}_w$	$\langle \ell/t \rangle_n$	$\langle \ell/t \rangle_w$	$\bar{\ell}_n/\bar{t}_n$[a]	$\bar{\ell}_w/\bar{t}_w$[b]
TPO	FD–ND	0.86	1.16	1.26	1.82	0.62	0.88	2.12	2.41	2.03	2.07
	TD–ND	0.85	1.16	1.14	1.58	0.66	0.98	1.82	1.99	1.72	1.62
0.84	FD–ND	0.60	0.86	0.87	1.55	0.44	0.69	2.07	2.60	1.98	2.24
	TD–ND	0.64	0.79	0.85	1.07	0.49	0.63	1.88	2.06	1.76	1.70
2.6	FD–ND	0.58	0.84	0.99	1.68	0.35	0.52	2.94	3.92	2.81	3.25
	TD–ND	0.55	0.73	0.77	1.06	0.39	0.58	2.10	2.37	1.97	1.83
4.7	FD–ND	0.53	0.77	0.99	1.46	0.28	0.33	3.98	5.24	3.48	4.45
	TD–ND	0.55	0.66	0.81	1.06	0.38	0.46	2.20	2.56	2.12	2.33
6.8	FD–ND	0.55	0.64	1.14	1.50	0.26	0.31	4.75	6.28	4.40	4.85
	TD–ND	0.59	0.65	0.91	1.06	0.40	0.44	2.38	2.73	2.29	2.41

[a] The values of the aspect ratio were computed from the number average particle length and thickness.
[b] The values of the aspect ratio were computed from the weight average particle length and thickness.

weight averages, obtained from views in the FD–ND plane and TD–ND plane for a series of nanocomposites containing various amounts of MMT and PP-*g*-MA is shown in Tables 3 and 4. As in the case of clay particles, the elastomer phase shows a sizeable distribution in particle lengths and thicknesses as well as in aspect ratios.

Fig. 12 shows the weight average apparent elastomer particle sizes, lengths and thicknesses as a function of MMT content obtained from AFM images viewed in the FD–TD plane and TD–ND plane. The data from the view in the FD–ND plane are taken from the previous paper [36], while those from the view in the TD–ND plane were obtained in this study. In the absence of MMT, the weight average elastomer particle size viewed in the TD–ND plane, $(\bar{d}_{TD-ND})_w$, in the TPO is 1.16 μm. A similar value is obtained from views in the FD–ND plane, $(\bar{d}_{FD-ND})_w$. However, the apparent particle size viewed parallel to the FD is somewhat smaller than that viewed parallel to the TD as the MMT content increases. It is expected that the particles viewed in the FD–ND plane would be

Table 4
Elastomer particle size comparison for TPO/PP-*g*-MA/MMT nanocomposites for different ratios of PP-*g*-MA/organoclay at a fixed MMT content of 5 wt%

PP-*g*-MA/organoclay	Plane of viewing	Particle size (μm)		Major length (μm)		Minor length (μm)		Elastomer aspect ratio			
		$\bar{d}_n$	$\bar{d}_w$	$\bar{\ell}_n$	$\bar{\ell}_w$	$\bar{t}_n$	$\bar{t}_w$	$\langle \ell/t \rangle_n$	$\langle \ell/t \rangle_w$	$\bar{\ell}_n/\bar{t}_n$[a]	$\bar{\ell}_w/\bar{t}_w$[b]
0	FD–ND	0.78	1.01	1.33	1.95	0.56	0.76	2.4	2.9	2.17	2.22
	TD–ND	0.64	0.77	0.89	1.17	0.47	0.57	1.93	2.10	1.91	2.06
0.5	FD–ND	0.76	1.01	1.2	1.69	0.47	0.65	3.02	3.74	2.81	3.03
	TD–ND	0.62	0.72	0.80	0.98	0.49	0.59	1.69	1.85	1.63	1.66
1.0	FD–ND	0.53	0.77	0.99	1.46	0.28	0.33	3.98	5.24	3.48	4.45
	TD–ND	0.55	0.66	0.81	1.06	0.38	0.55	2.20	2.56	2.12	2.33
2.0	FD–ND	0.51	0.65	1.04	1.7	0.26	0.35	4.42	6.53	3.93	4.82
	TD–ND	0.60	0.66	0.84	0.97	0.44	0.48	1.98	2.23	1.92	2.00

[a] The values of the aspect ratio were computed from the number average particle length and thickness.
[b] The values of the aspect ratio were computed from the weight average particle length and thickness.

larger in size or longer in length than those viewed in the TD–ND plane due to the flow field during the injection-molding process. Similar trends in average length, $\bar{\ell}_{FD}$ or $\bar{\ell}_{TD}$ (major axis), and thickness, $\bar{t}_{ND,view||TD}$ or $\bar{t}_{ND,view||FD}$ (minor axis), of elastomer particles as viewed in the two directions are also apparent, see Fig. 12(b). Interestingly, the thickness seems independent of the viewing direction; whereas, the elastomer particle length along the FD is somewhat greater than that along the TD because of the elongation of elastomer particles along the FD by the flow field. There are slight differences in the thickness of particles at high MMT content, e.g., 5 and 7 wt%, obtained from the two viewing planes; this suggests that the elastomer particles may not be exactly ellipsoidal in shape. This may stem in part from the viewing plane not exactly matching the orthogonal coordinates of the molded bar. However, clearly, the elastomer particles have complex shapes owing to the effect that the clay particles have on them as further discussed below [14,36,45].

The apparent elastomer particle size seen in a view in FD–ND plane decreases rather strongly as the PP-*g*-MA/organoclay ratio increases; whereas, the size obtained from views in the TD–ND

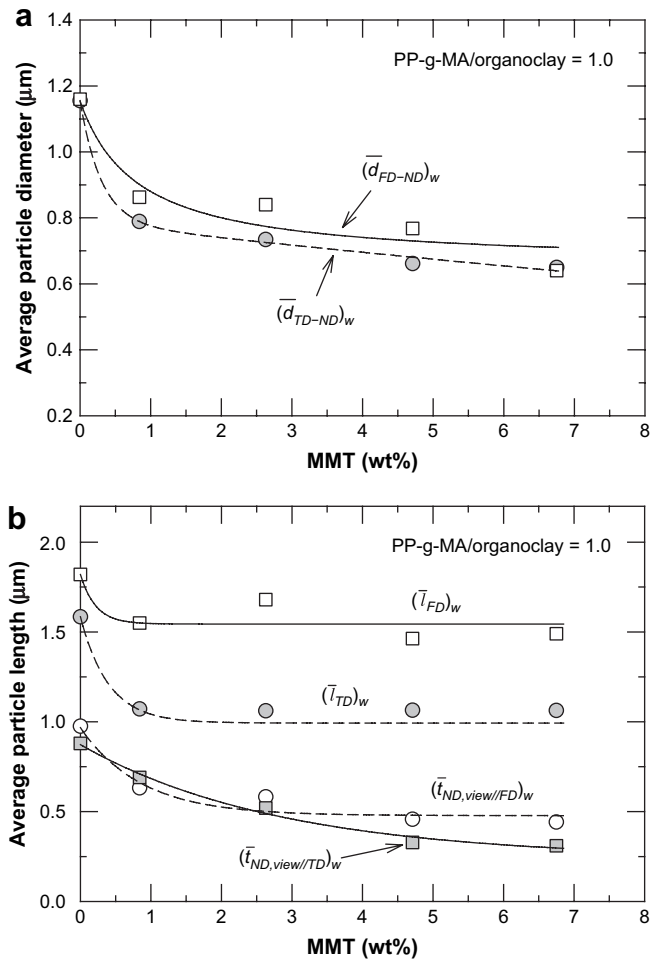

Fig. 12. Comparison of average particle diameter (a) and length and thickness (b) of elastomer particles for TPO/PP-*g*-MA/MMT nanocomposites as a function of MMT content in the different flow directions.

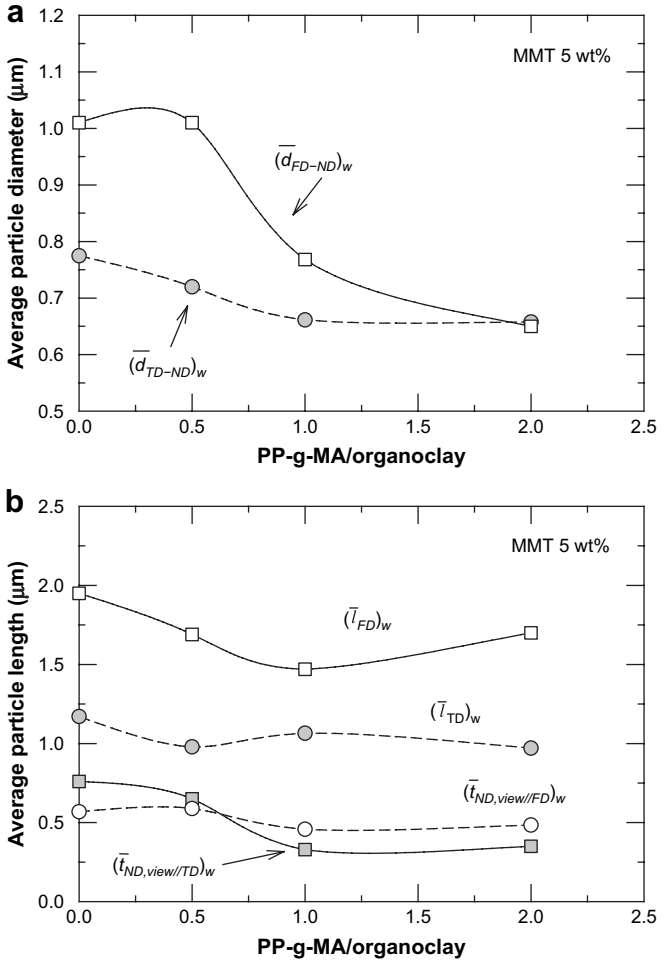

Fig. 13. Comparison of average particle diameter (a) and length and thickness (b) of elastomer for TPO/PP-*g*-MA/MMT nanocomposites as a function of PP-*g*-MA/organoclay ratio in the different flow directions.

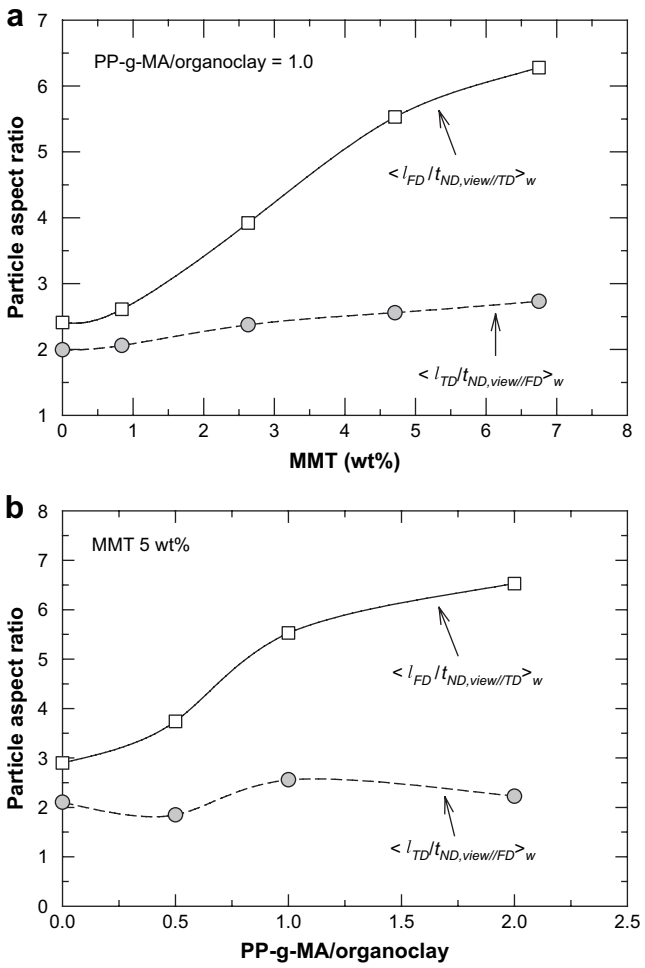

Fig. 14. Comparison of particle aspect ratio of elastomer for TPO/PP-*g*-MA/MMT nanocomposites as a function of MMT (a) and PP-*g*-MA/organoclay ratio (b) in the different flow directions.

plane decreases relatively less as shown in Fig. 13(a). Fig. 13(b) shows that the elastomer particle length and thickness are not strongly affected by the PP-*g*-MA/organoclay ratio, but, in general, these dimensions decrease as the PP-*g*-MA/organoclay ratio increases. The average aspect ratios, e.g., $\langle \ell_{FD}/t_{ND,view||TD}\rangle_w$ and $\langle \ell_{TD}/t_{ND,view||FD}\rangle_w$, shown in Fig. 14 reveal a strong directional dependence of the particle shapes. The particle aspect ratios increase significantly with the addition of clay and increased PP-*g*-MA/organoclay ratio when viewed in the FD–ND plane while they do not change much when viewed in the TD–ND plane. It has been well documented in previous studies that the size of the dispersed polymer phase in blends is decreased by the presence of clay particles or platelets [14,36,45]. While several factors may be involved, the evidence strongly supports the idea that the presence of clay platelets between elastomer particles significantly reduces the rate of their coalescence; this shifts the balance of droplet break-up versus coalescence leading to smaller elastomer particles in the blend. It would seem reasonable that this so-called "barrier" effect would become greater as the density of clay particles increases, i.e., as the clay becomes better dispersed. This is consistent with the current observation that elastomer particle size decreases as the PP-*g*-MA/organoclay ratio increases causing more organoclay particles to be formed. The elastomer particles also become more elongated and oriented as the PP-*g*-MA ratio increases. It should be noted that the clay particles are mainly oriented in the direction of flow, and it appears that this results in the elongation of the elastomer particles along the FD. The deformed elastomer particles within injection-molded specimens seem to play an important role in the thermal expansion behavior of the current nanocomposites as will be discussed in more detail later.

3.2. Linear thermal expansion behavior of nanocomposites

As explained in Section 2, the thermal expansion behavior of the nanocomposite specimens was recorded over a broad temperature range (up to 125 °C); however, the thermal expansion over the range of 0–30 °C is of particular interest since we relate the results to the mechanical properties measured at room temperature, i.e., ca. 25 °C, as will be discussed in more detail in a subsequent paper. Thus, all data presented in this paper were obtained over the 0–30 °C temperature range from the second heating scan of these nanocomposites. Further details of thermal expansion measurements are given in a previous paper [14].

Fig. 15 shows the linear thermal expansion coefficients, or CTEs, measured in all directions for TPO-based nanocomposites as a function of MMT content at various PP-*g*-MA/organoclay ratios. As expected, the CTE along the FD and the TD decreases as MMT content increases; whereas, the CTE along the ND increases as MMT content increases. The increase in CTE in the ND for injection-molded polymer blends is a result of the reduced expansion in the FD and TD. It is noted that the CTEs in the TD and ND (Fig. 15(b) and (c)) for the pure TPO are higher than that in the FD (Fig. 15(a)) due to polymer chain and/or crystallite orientation resulting from the injection-molding process. The change in CTE when the organoclay is added to TPO without any PP-*g*-MA present is relatively small regardless of the direction of measurement. The addition of even a small amount of PP-*g*-MA causes significant reductions in CTE for the FD and TD; however, the absolute amount of change over the range of PP-*g*-MA/organoclay ratios from 0.5 to 2 seems to lead to only marginal differences. This point is made more clear from plots of CTE versus the PP-*g*-MA/organoclay ratio at fixed MMT content.

As shown in Fig. 16, the addition of a small amount of PP-*g*-MA causes significant reductions in CTE in the FD and the TD, but the rate of decrease diminishes at higher ratios. On the contrary, thermal expansion in the ND, Fig. 16(c), increases at low PP-*g*-MA/organoclay ratios and decreases at higher ratios. Figs. 15(d) and 16(d) show that the bulk expansion coefficient, obtained by adding the measured CTEs in the three directions, i.e., $\alpha_{bulk} = \alpha_{FD} + \alpha_{TD} + \alpha_{ND}$, is relatively unaffected by MMT content and PP-*g*-MA/organoclay ratio but decreases slightly with high amounts of clay and PP-*g*-MA. We note there are several factors that play roles in opposition to each other as discussed by Lee et al. [14]: (1) there are morphological rearrangements in the ternary system, i.e., the clay affects elastomer morphology and vice versa. (2) Since the PP-*g*-MA has a higher thermal expansion coefficient than TPO or MMT, thermal expansion tends to increase as more PP-*g*-MA is added; whereas, the well-dispersed clay particles by the addition of PP-*g*-MA reduce the thermal expansion. (3) Adding PP-*g*-MA lowers the modulus and a lower modulus of the matrix makes it easier for MMT to restrain the expansion of the composite.

A better understanding of the thermal expansion behavior of these nanocomposites can be obtained by normalizing the CTE data in the FD and TD discussed above by the CTE of the corresponding polymer matrix, i.e., α_m of TPO and TPO/PP-*g*-MA blends without any organoclay. Thus, the linear thermal expansion coefficients (CTEs) in all directions for TPO/PP-*g*-MA blends without any clay were measured with the results shown in Fig. 17. Interestingly, the CTE in the FD is more or less constant at low PP-*g*-MA contents (<10 wt%) and then increases at higher PP-*g*-MA contents. The eventual increase is inevitable since PP-*g*-MA has a higher thermal

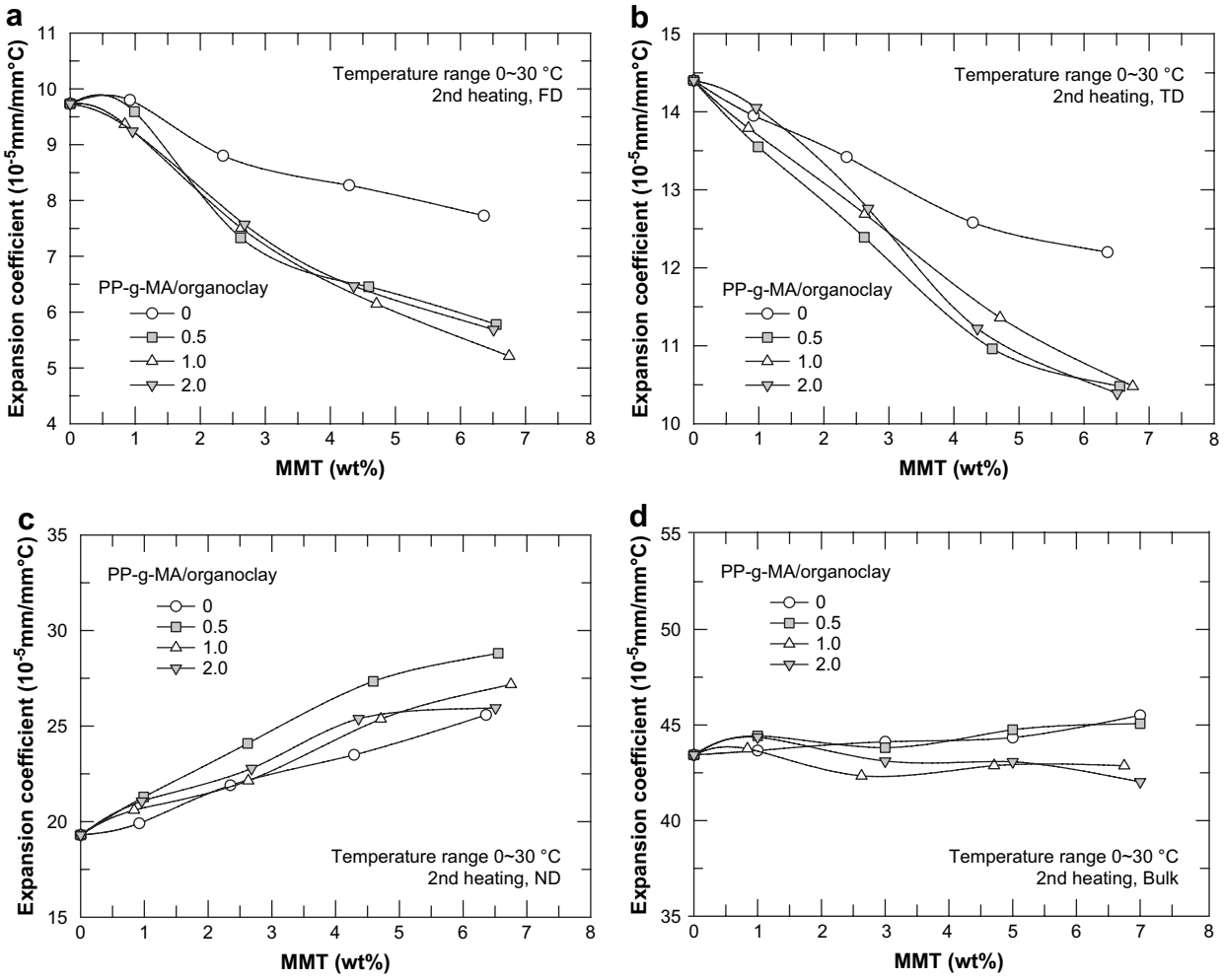

Fig. 15. Linear thermal expansion coefficient for TPO/PP-*g*-MA/MMT nanocomposites as a function of MMT content in different directions: flow (a), transverse (b), normal directions (c) and bulk expansion coefficients (d).

expansion coefficient than TPO. On the other hand, the CTEs along the TD and the ND show a slight increase at low PP-*g*-MA content and then decrease at higher contents. The bulk thermal expansion coefficient is relatively independent of the blend composition. As with the mechanical properties for these materials [36], the presence of PP-*g*-MA without clay or clay without PP-*g*-MA, i.e., large tactoids, does not significantly affect the thermal expansion of TPO even though there is directional dependence as shown above. Addition of PP-*g*-MA to TPO without any organoclay present does not significantly affect the morphology of the dispersed elastomer phase in the TPO or the thermal expansion behavior of the TPO matrix. On the other hand, organoclay without any PP-*g*-MA does not seem to affect the thermal expansion of the TPO significantly (see Figs. 15 and 16).

The normalized CTE values are plotted as a function of the PP-*g*-MA/organoclay ratio in Fig. 18. For a clear comparison of the two methods, the solid lines represent the nanocomposite CTE data normalized by the CTE of the TPO/PP-*g*-MA matrix while the symbols correspond to normalization by the CTE of the TPO alone. The normalized CTE in the FD decreases with increasing PP-*g*-MA/organoclay ratio regardless of the normalization method as shown in Fig. 18(a). Interestingly, at the low PP-*g*-MA/organoclay ratio, or low MMT content, the method of normalization does not matter; however, normalization by the CTE of the TPO/PP-*g*-MA matrix leads to lower values at the higher PP-*g*-MA/organoclay ratios. It is important to note that adding PP-*g*-MA lowers the modulus which makes it easier for the filler to restrain the expansion of the composite; however, the main effect of the PP-*g*-MA is to increase the filler aspect ratio and make it easier to orient to the flow direction by increasing the degree of exfoliation. However, the extent of reduction in CTE along the TD shows an opposite trend. The normalized CTE along the TD decreases at low PP-*g*-MA/organoclay ratio and then increases at higher ratios (see Fig. 18(b)). This anisotropic thermal expansion behavior may be due to the changes in the morphology of clay and elastomer particles, that is, the increase of the orientation of well-dispersed clay platelets and highly elongated elastomer particles with smaller particle sizes along the FD by adding more PP-*g*-MA. This was shown in the morphology and particle analysis presented in this and previous papers [36].

Recently, significant reductions in CTE were observed in polymer/rubber blends, e.g., PP/EPR, PA/EPR, PP/EOR, etc., when the rubber domains were highly deformed into micro-layer or co-continuous structures [46,47], especially for blends containing high rubber concentrations, e.g., >40% [47]. The morphological changes of the rubber phase were achieved by controlling the rubber concentration and processing conditions. However, this is not the case for the current nanocomposites because of the presence of the organoclay. Lee et al. [14] observed the significant reduction of CTE for PP/elastomer nanocomposites by changing the amount of MMT and elastomer. They reported that a higher extent of constraint and the resulting reduction in CTE are only achieved when the

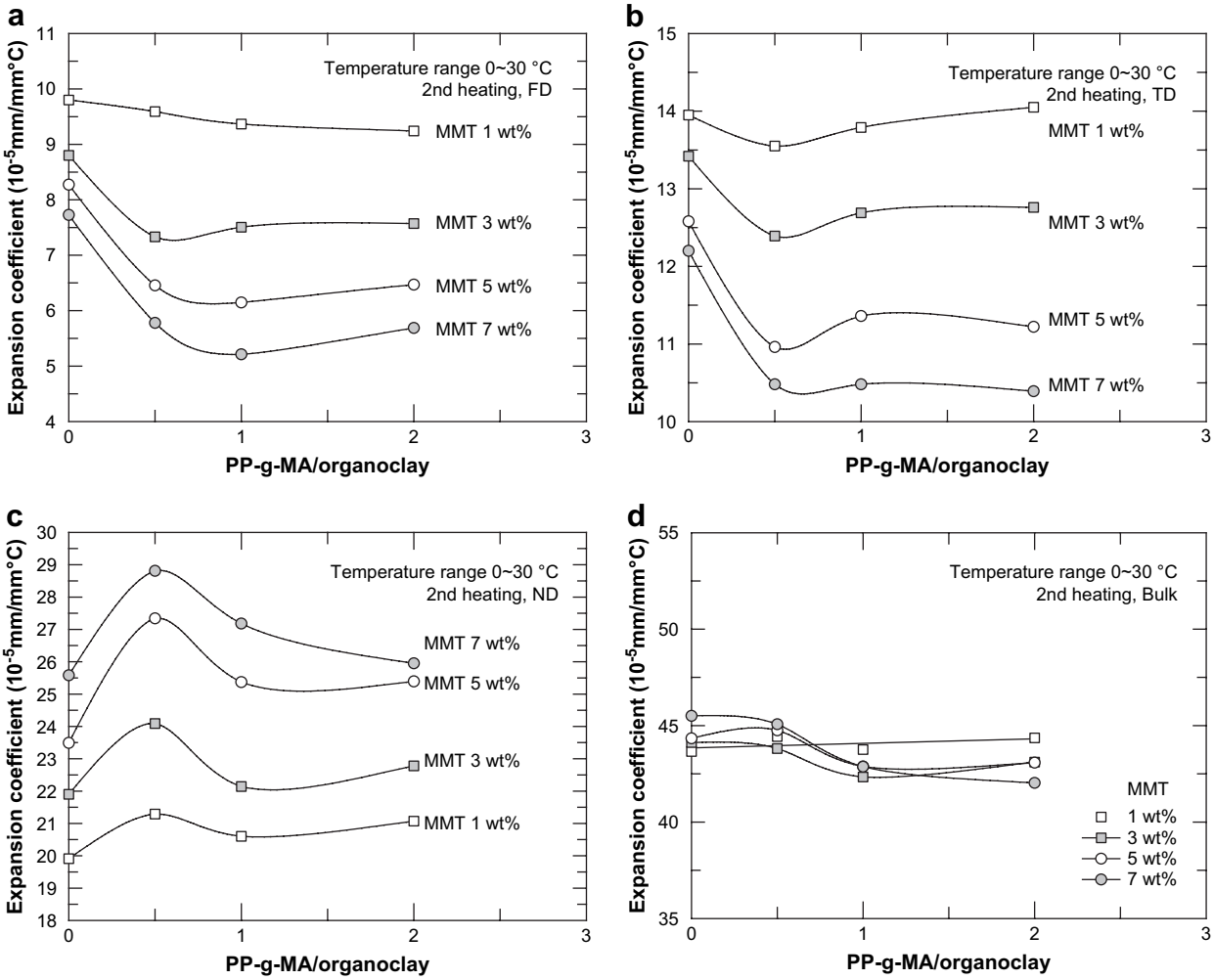

Fig. 16. Linear thermal expansion coefficient for TPO/PP-*g*-MA/MMT nanocomposites as a function of PP-*g*-MA/organoclay ratio in different directions: flow (a), transverse (b), normal directions (c) and bulk expansion coefficients (d).

elastomer particles are well-dispersed with highly elongated shapes in the nanocomposites containing higher elastomer, e.g., 30 or 40%, and MMT contents, e.g., 7% at a fixed PP-*g*-MA/organoclay ratio of 1.0 [14]. For current nanocomposites containing a fixed amount of elastomer, e.g., 25% [36], well-dispersed and highly elongated elastomer particles can be achieved at higher PP-*g*-MA/organoclay ratio of 2.0, resulting in the significant reduction of CTE as shown in Fig. 18(a).

4. Summary and conclusions

The ratio of PP-*g*-MA to organoclay strongly affects the morphology of the clay platelets and the elastomer particles with consequent changes in thermal expansion characteristics. An in-depth particle analysis of the morphology of each by TEM (clay) and AFM (elastomer) along the FD and TD of injection-molded specimens revealed that the anisotropy of both the clay and the elastomer particles is highly dependent on the MMT concentration and/or PP-*g*-MA/organoclay ratio in the nanocomposites. Both average length and thickness of the clay particles viewed parallel to the FD and the TD decreased with increasing PP-*g*-MA/organoclay ratio, resulting in an increase of the aspect ratio of clay particles. However, the aspect ratio along the FD was higher than that along the TD. On the other hand, the aspect ratio of elastomer particles along the FD was much higher than that along the TD. Furthermore, highly elongated particles along the FD were observed at high PP-*g*-MA/organoclay ratios. This combined effect of the mechanical constraint by the organoclay and the highly elongated elastomer particles at high PP-*g*-MA contents leads to significant reductions in thermal expansion for these materials.

The increase of the PP-*g*-MA/organoclay ratio tends to significantly reduce the thermal expansion in both FD and TD of injection-molded specimens; however, the extent of reduction of CTE in the FD is much greater than that in the TD, especially as the amount of PP-*g*-MA is increased. On the other hand, thermal expansion in the ND slightly increased as MMT content is increased. As expected, the bulk expansion coefficient is not strongly affected by MMT content and/or PP-*g*-MA/organoclay ratio.

The important effects of increasing the PP-*g*-MA content include increasing the number of organoclay particles, i.e., improving dispersion, increasing the aspect ratio of the clay particles, and improving their orientation in the flow field. These benefits to morphology and subsequently to performance become marginal beyond a PP-*g*-MA/organoclay ratio of about 1. While the benefits of adding PP-*g*-MA are large, it is clear that the current materials are still rather far from full exfoliation and the ultimate performance that potentially might be achieved. The current results provide a better understanding of the influence of the PP-*g*-MA/organoclay ratio on the relationship between composite morphology and CTE behavior needed to achieve improved

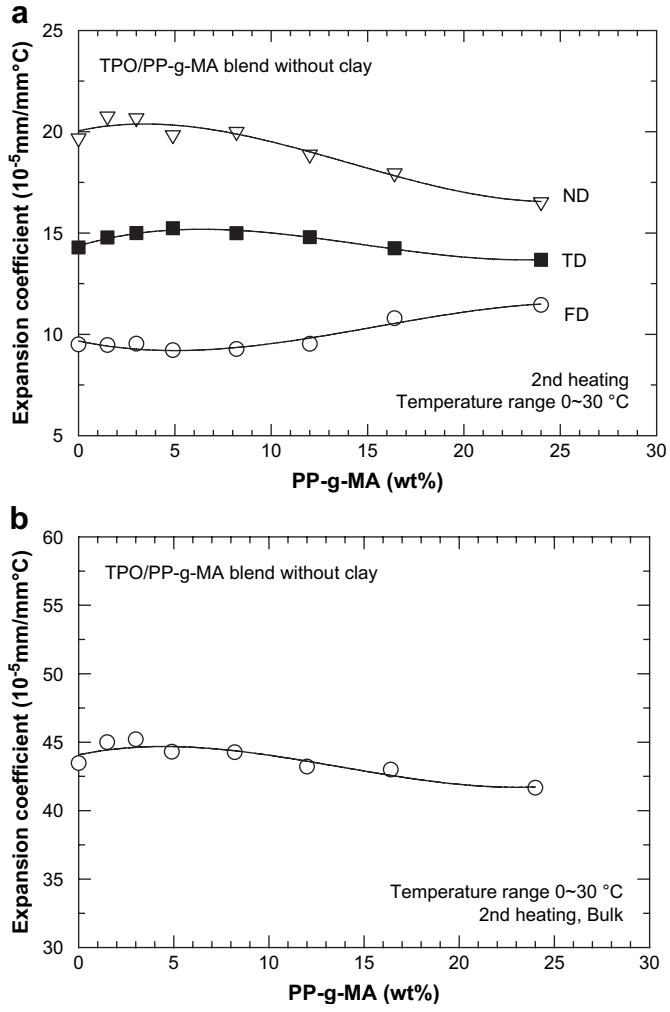

Fig. 17. Linear thermal expansion coefficient for TPO/PP-*g*-MA blends without clay in different directions: (a) flow, transverse and normal directions and (b) bulk expansion coefficient.

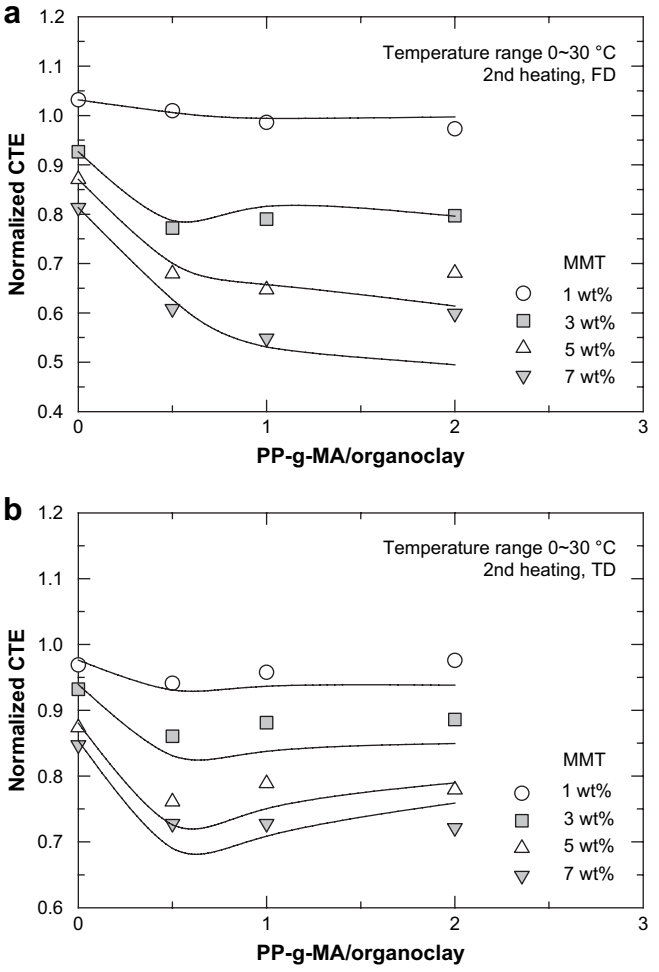

Fig. 18. Normalized CTEs for TPO-based nanocomposites as a function of PP-*g*-MA/organoclay ratios in different directions: (a) flow and (b) transverse directions. Solid lines indicate the nanocomposite CTE data normalized by the CTE of the TPO/PP-*g*-MA matrix and the symbols correspond to normalization by the CTE of TPO.

dimensional stability of injection-molded parts from TPO-based nanocomposites.

Acknowledgements

The authors thank General Motors for funding this work and the permission to publish it. The authors would like to thank Dr. Douglas Hunter and Dr. P.J. Yoon of Southern Clay Products for technical assistance and for providing materials.

References

[1] Usuki A, Kojima Y, Kawasumi M, Okada A, Fukushima Y, Kurauchi T, et al. J Mater Res 1993;8(5):1179–84.
[2] Kojima Y, Usuki A, Kawasumi M, Okada A, Fukushima Y, Kurauchi T, et al. J Mater Res 1993;8(5):1185–9.
[3] Alexandre M, Dubois P. Mater Sci Eng R Rep 2000;28(1–2):1–63.
[4] Garces JM, Moll DJ, Bicerano J, Fibiger R, McLeod DG. Adv Mater 2000;12(23):1835–9.
[5] Giannelis EP. Adv Mater 1996;8(1):29–35.
[6] Hussain F, Hojjati M, Okamoto M, Gorga RE. J Compos Mater 2006;40(17):1511–75.
[7] Ray SS, Okamoto M. Prog Polym Sci 2003;28(11):1539–641.
[8] Brandrup J, Immergut E. Polymer handbook. 3rd ed. New York: Wiley; 1989. p. V27–V33.
[9] Segal L. Polym Eng Sci 1979;19(5):365–72.
[10] Holliday L, Robinson J. J Mater Sci 1973;8(3):301–11.
[11] Chow TS. J Polym Sci Polym Phys Ed 1978;16(6):967–70.
[12] Okada A, Usuki A. Mater Sci Eng C Biomim Mater Sens Syst 1995;C3(2):109–15.
[13] Yoon PJ, Fornes TD, Paul DR. Polymer 2002;43(25):6727–41.
[14] Lee H-S, Fasulo PD, Rodgers WR, Paul DR. Polymer 2006;47(10):3528–39.
[15] Fasulo PD, Rodgers WR, Ottaviani RA, Hunter DL. Polym Eng Sci 2004;44(6):1036–45.
[16] Engberg K, Ekblad M, Werner P, Gedde U. Polym Eng Sci 1994;34:1340–53.
[17] Kaji M, Nakahara K, Ogami K, Endo T. J Appl Polym Sci 2000;75(4):528–35.
[18] Yakushin VA, Stirna UK, Zhmud NP. Mech Compos Mater 2000;35(4):351–6.
[19] Ashton J, Halphin J, Petit P. Structure property relationship for composite materials, Primer composite material analysis. Lancaster: Technomic; 1969.
[20] Kim DH, Fasulo PD, Rodgers WR, Paul DR. Polymer 2007;48(18):5308–23.
[21] Ellis TS, D'Angelo JS. J Appl Polym Sci 2003;90(6):1639–47.
[22] Galgali G, Ramesh C, Lele A. Macromolecules 2001;34(4):852–8.
[23] Hambir S, Bulakh N, Jog JP. Polym Eng Sci 2002;42(9):1800–7.
[24] Ishida H, Campbell S, Blackwell J. Chem Mater 2000;12(5):1260–7.
[25] Kim DH, Cho KS, Mitsumata T, Ahn KH, Lee SJ. Polymer 2006;47(16):5938–45.
[26] Kim DH, Park JU, Ahn KH, Lee SJ. Macromol Rapid Commun 2003;24(5–6):388–91.
[27] Kodgire P, Kalgaonkar R, Hambir S, Bulakh N, Jog JP. J Appl Polym Sci 2001;81(7):1786–92.
[28] Lertwimolnun W, Vergnes B. Polymer 2005;46(10):3462–71.
[29] Marchant D, Jayaraman K. Ind Eng Chem Res 2002;41(25):6402–8.
[30] Nam PH, Maiti P, Okamoto M, Kotaka T, Hasegawa N, Usuki A. Polymer 2001;42(23):9633–40.
[31] Park JU, Kim JL, Kim DH, Ahn KH, Lee SJ, Cho KS. Macromol Res 2006;14(3):318–23.
[32] Reichert P, Hoffmann B, Bock T, Thomann R, Mulhaupt R, Friedrich C. Macromol Rapid Commun 2001;22(7):519–23.
[33] Hasegawa N, Okamoto H, Kawasumi M, Kato M, Tsukigase A, Usuki A. Macromol Mater Eng 2000;280/281:76–9.

[34] Mehta S, Mirabella FM, Rufener K, Bafna A. J Appl Polym Sci 2004;92(2):928–36.
[35] Mishra JK, Hwang KJ, Ha CS. Polymer 2005;46(6):1995–2002.
[36] Kim DH, Fasulo PD, Rodgers WR, Paul DR. Polymer 2007;48(20–21):5960–78.
[37] Fornes TD, Paul DR. Polymer 2003;44(17):4993–5013.
[38] Chavarria F, Paul DR. Polymer 2004;45(25):8501–15.
[39] Chavarria F, Paul DR. Polymer 2006;47(22):7760–73.
[40] Vaia RA, Giannelis EP. MRS Bull 2001;26(5):394–401.
[41] Yalcin B, Cakmak M. Polymer 2004;45(19):6623–38.
[42] Park H-M, Liang X, Mohanty AK, Misra M, Drzal LT. Macromolecules 2004;37(24):9076–82.
[43] Fornes TD, Hunter DL, Paul DR. Polymer 2004;45(7):2321–31.
[44] Lee H-S, Fasulo PD, Rodgers WR, Paul DR. Polymer 2005;46(25):11673–89.
[45] Khatua BB, Lee DJ, Kim HY, Kim JK. Macromolecules 2004;37(7):2454–9.
[46] Ono M, Washiyama J, Nakajima K, Nishi T. Polymer 2005;46(13):4899–908.
[47] Wu G, Nishida K, Takagi K, Sano H, Yui H. Polymer 2004;45(9):3085–90.